

Article

Investigation of 3 dB Optical Intensity Spot Radius of Laser Beam under Scattering Underwater Channel

Wei Wang ^{1,2}, Xiaoji Li ^{1,2,*}, Sujan Rajbhandari ³ and Yanlong Li ¹

¹ Ministry of Education Key Laboratory of Cognitive Radio and Information Processing, Guilin University of Electronic Technology, Guilin 541004, China; baiyunchuxiu2019@outlook.com (W.W.); lyulong@guet.edu.cn (Y.L.)

² Guangxi Experiment Center of Information Science, Guilin 541004, China

³ Institute of Future Transport and Cities, School of Computing, Electronics and Mathematics, Coventry University, Coventry CV15FB, UK; sujan.rajbhandari@coventry.ac.uk

* Correspondence: lixj@guet.edu.cn; Tel.: +86-0773-356-2830

Received: 24 November 2019; Accepted: 8 January 2020; Published: 11 January 2020



Abstract: An important step in the design of receiver aperture and optimal spacing of the diversity scheme for an underwater laser communication system is to accurately characterize the two-dimensional (2D) spatial distribution of laser beam intensity. In this paper, the 2D optical intensity distribution and 3 dB optical intensity spot radius (OISR) are investigated due to the dominating optical intensity of laser beam being within the 3 dB OISR. By utilizing the Henyey–Greenstein function to compute the scattering angles of photons, the effects of the scattering underwater optical channel and optical system parameters on 3 dB OISR are examined based on the Monte Carlo simulation method. We have shown for the first time that in the channel with a high density of scattering particles, the divergence angle of the laser source plays a negligible role in 3 dB OISR. This is an interesting phenomenon and important for optical communication as this clearly shows that the geometric loss is no longer important for the design of receiver aperture and optimal spacing of the diversity scheme for the underwater laser communication system in the highly scattering channel.

Keywords: 3 dB optical intensity spot radius; scattering underwater channel; Monte Carlo simulation method

1. Introduction

There had been significant interest in underwater communication for ocean exploration, environment monitoring, diver safety and other applications. Currently, acoustic, radio frequency (RF) and optical communications are considered for underwater communication. The underwater acoustic communication system suffers from limited bandwidth. Hence it is not suitable for high-speed communication. The RF spectrums suffer from extremely high attenuation in oceanic environments, limiting the communication to a very short distance. The various studies have already proven that the optical spectrum between blue and green wavelengths is one of the most suitable media to transfer information in the underwater channel due to its high bandwidth and low attenuation [1–3].

There are a number of studies that characterized the underwater optical channel in terms of channel attenuation, channel impulse response (CIR) and signal distribution in spatial domain using the Monte Carlo (MC) simulation method, vector radiative transfer (VRT) theory, beam spread function (BSF), radiative transfer equation (RTE), stochastic model, closed expression model, numerical model, modified Beer–Lambert (BL) law and experimental measurement. Table 1 summarizes the aforementioned methods used for characterizing the underwater optical communication and their contributions.

Table 1. Survey of recent underwater optical channel modeling.

Ref. No.	Methods	Contribution Highlights
[4]	VRT theory	Path losses. Received waveform degradation. Link bit error rate.
[5]	BSF	Optical power distribution on the receiving plane.
[6–8]	Experiments	Modulation depth, degree of polarization of modulated light.
[9]	MC	CIR. Channel capacity.
[10]	MC	Path losses. CIR. Bit error rate. Received photons distribution.
[11]	Experiments	Effects of misalignment, scattering agents on temporal response.
[12]	MC	Path losses for various channel configurations.
[13]	MC	Wavelength-dependent path losses based on the bio-optical model of seawater given by [14].
[15]	RTE	Path losses modeled by direct RTE solver.
[16]	Closed expression	CIR modeled by double gamma functions.
[17]	Closed expression	MIMO CIR modeled by weight gamma function polynomial.
[18]	Stochastic model	Spatial and temporal probability characteristics of photons.
[19]	Closed expression	Path losses modeled by weighted function of two exponentials.
[20]	MC	CIR and normalized received optical power.
[21]	MC	Different effects of two scattering angle computational principle on CIR.
[22]	Experiments	Statistical distribution of optical intensity fluctuations caused by temperature-induced oceanic turbulence.
[23]	MC	Probability density function of oceanic turbulence channel.
[24]	MC	Turbulence-induced scintillation index and path losses.
[25]	MC	Empirical model of transmission distance-dependent path losses.
[26]	MC	Channel estimation and evaluation under geometric losses.
[27]	MC	Scattering regimes of photons.
[28]	Experiments	Optical receiving power, CIR based on a newly developed scattering phase function which better fit for real seawater.
[29]	Closed expression	Statistical model of intensity fluctuations caused by random temperature and salinity variations and air bubbles. Channel coherence time.
[30]	Ray tracing	New CIR model that is superior to the weighted double gamma functions.
[31]	Modified BL law	CIR and path losses for blocking and shadowing channel.
[32]	Experiments	Path losses.
[33]	Numerical Model	Air bubble and temperature gradient-induced channel irradiance fluctuations presented by mixture exponential-generalized gamma distribution.
[34]	BSF	Influences of group velocity dispersion and time jitter at the pulse width, probability fade and maximum bit rate.
[35]	RTE	Lower mathematical complexity and simplicity.
[36]	Experiments	Improved accurate solver for time-dependent RTE.
[37]	Experiments	Beam's wave-front distortion caused by turbulence. Real-time associated Zernike coefficients. Transmission of polarized light and light with OAM.
[37]	Experiments	Impacts of temperature gradient-induced turbulence, population and size of air bubbles on non-line-of-sight channel.

None of these works, however, characterize the two-dimensional (2D) spatial distribution of the laser beam on the receiving plane. The laser beams in the underwater channel experience significant random scattering. Hence, compared with the natural divergence, laser beams at the receiving plane in the underwater channel have a larger optical spot. However, the real optical receiver's aperture tends to be significantly smaller than the whole beam spot under the scattering underwater channel. The knowledge of optical intensity distribution on the receiving plane with finite dimensions is important for designing the optical receiver aperture and optimal spacing between receivers for the spatial diversity scheme. Hence, in this paper, the optical intensity distribution of the laser beam on the receiving plane in the scattering underwater medium is studied for the first time.

In order to characterize the underwater optical channel, we defined and calculated 3 dB optical intensity spot radius (OISR) at the receiver's plane as the dominating optical power of the laser beam be within the 3 dB OISR. The MC simulation method is often used to study the radiance transfer equation of optical waves' propagation in the scattered media and also applied to trace the trajectory of photons. Compared with the experimental measurements, the MC approach offers flexibility

to alter the optical channel and system parameters. More importantly, it can reveal the statistical characteristics of underwater optical channel accurately because an enormous number of photons are counted [9,10,12]. Hence, based on the MC simulation method, the investigation on the effects of underwater channel and optical system parameters (such as the channel type, half-aperture size of receiving plane with finite dimensions, transmission distance and divergence angle) on the 3 dB OISR is very important for the design of receiver aperture and optimal spacing of spatial diversity scheme for an underwater laser communication system. The results show that in a highly scattering channel (such as harbor seawater channel) the optical intensity distribution is no longer a Gaussian and the effects of the divergence angle on 3 dB OISR is negligible i.e., the geometric loss is no longer important for the design of receiver aperture and optimal spacing of the diversity scheme in the highly scattering underwater communication channel.

The rest of the paper is organized as follows: Section 2 describes the principle of the MC simulation method, the computational principle of 3 dB OISR is given in Section 3, simulation results and analysis are presented in Section 4 and followed by conclusions in Section 5.

2. Monte Carlo Simulation Method

To adopt the MC simulation method to trace the propagation trajectory of photons in seawater, six key parameters of photons are considered: (a) Coordinates $(x_0, y_0, z_0) = (r_0 \cos \psi_0, r_0 \sin \psi_0, 0)$; (b) zenith angle $(\theta_0 = T - \text{Phai} \sqrt{-\ln(1 - \zeta_1)/2})$; (c) azimuth angle $(\psi_0 = 2\pi\zeta_2)$ for photons emission; (d) propagation distance (d) ; (e) zenith angle (θ_s) and (f) azimuth angle (ψ_s) for each scattering event [20]. Here $r_0 = w_0 \sqrt{-\ln(1 - \zeta_3)}$ is the distance of emission photons to the geometric center of the laser source, w_0 is the beam waist radius and $T - \text{Phai}$ is the divergence angle of the laser beam; ζ_1 , ζ_2 and ζ_3 are random number uniform on $[0, 1]$.

2.1. Scattering Phase Function

Unlike the free space atmospheric environments, seawater contains massive phytoplankton, dissolved salts, mineral particles and dissolved organic matter, which induces absorption and scattering effects on the laser beam, particularly for the coastal and harbor underwater optical channel. To model the scattering of the laser beam caused by suspended particles, the volume scattering function (VSF) $\bar{\beta}(\theta, \lambda)$ is used to characterize the scattered intensity per unit incident irradiance per unit volume of water. Assume the laser beam to be unpolarized and the seawater to be isotropic, and hence the scattering becomes angular dependent. It is presented as a fraction of scattered out intensity of the laser beam through an angle θ into a solid angle $\Delta\Omega$, and the VSF is given as [1,3]:

$$\bar{\beta}(\theta, \lambda) = \lim_{\Delta r \rightarrow 0} \lim_{\Delta\Omega \rightarrow 0} \frac{P_s(\theta, \lambda)}{P_i(\theta, \lambda) \Delta r \Delta\Omega} \quad (1)$$

where θ is the scattering angle of photons, $P_s(\theta, \lambda)$ is the scattered optical power through θ into $\Delta\Omega$, $P_i(\theta, \lambda)$ is the incident optical power, λ is the wavelength of the laser beam and Δr is the seawater thickness. By integrating the $\bar{\beta}(\theta, \lambda)$ over all angles, the scattering coefficient $K_s(\lambda)$ is obtained as [1,3]:

$$K_s(\lambda) = \int_{4\pi} \bar{\beta}(\theta, \lambda) d\theta = 2\pi \int_0^\pi \bar{\beta}(\theta, \lambda) \sin\theta d\theta \quad (2)$$

The scattering phase function (SPF) is used to describe the probability distribution of propagation direction of the scattered photons. Normalizing Equation (1) with $K_s(\lambda)$, the SPF is expressed as [1,3]:

$$\beta(\theta, \lambda) = \frac{\bar{\beta}(\theta, \lambda)}{K_s(\lambda)} \quad (3)$$

There are various SPF models to represent the scattering characteristics of seawater channels, such as the Fournier–Forand function, the Henyey–Greenstein (HG) function and their modifications.

Among the above-mentioned SPF functions, only the HG function can establish analytical expression between the scattering angles and the random numbers [20]. This is in favor of improving the computational accuracy and reducing the computational complexity in simulation analysis. While the HG function fails to provide very accurate results for photon scattering with small and large angles, such deviations are considered acceptable in the theoretical analysis [38]. Hence, in this paper, we adopt the HG function as SPF to compute the scattering angles, which satisfies the following equation:

$$1 = \int_0^\pi \beta(\theta, \lambda) \sin \theta d\theta \quad (4)$$

where $\beta(\theta, \lambda)$ is the SPF, θ is the scattering angle of photons and λ is the wavelength of the laser beam. In this paper, a fixed wavelength λ of 532 nm is selected. Hence, $\beta(\theta, \lambda)$ can be replaced by $\beta(\theta)$, and the expression of the HG function is given by [39]:

$$\beta_{HG}(\theta) = \frac{1 - g^2}{4\pi(1 + g^2 - 2g \cos \theta)^{-3/2}} \quad (5)$$

where g is the asymmetry parameter (equal to the average cosine of the scattering angle over all scattering angles).

2.2. Photon Propagation

2.2.1. Propagation Distance

According to the definition of optical distance L and the Beer Law, the probability density function for the intensity attenuation of the laser beam as a function of L is given by [39–41]:

$$p_L(L) = \exp(-L), L > 0 \quad (6)$$

Hence, the probability that a photon is absorbed and scattered between an optical distance 0 to L is given by [39–41]:

$$P_L(L) = \int_0^L p_L(l) dl = \xi_4 \quad (7)$$

where is the probability of photons travel over an optical distance of L , and $P_L(L) = \xi_4$ is a random number uniform on $[0,1]$. Consequently, $L = -\ln(1 - \xi_4)$, due to $L = K_{att}(\lambda)d$, $K_{att}(\lambda)$ is the attenuation coefficient. Hence, the photons propagation distance for each scattering event can be solved by:

$$d = -\ln(1 - \xi_4)/K_{att}(\lambda) \quad (8)$$

2.2.2. Photon Weight

As the laser beam propagates over a distance in the seawater channel, a certain percentage of photon energy is absorbed and the rest is scattered. The energy weight of photon after scattering is given by:

$$w_{post} = \mu w_{pre} \quad (9)$$

where $\mu = K_s(\lambda)/K_{att}(\lambda)$ is the albedo, w_{pre} and w_{post} are the pre-scattering and post-scattering energy weight, respectively. Each time the photon is scattered, the energy weight survival rate is μ . In this paper, initial energy weight is assumed to be 1. To improve computation time, $w_{post} = 10^{-10}$ is set as the photon's survival threshold, i.e., $w_{post} < 10^{-10}$, the propagating photons are annihilated.

2.2.3. Propagation Direction

According to θ_0 and ψ_0 for photon emission, $(\mu_{x_0}, \mu_{y_0}, \mu_{z_0}) = (\sin\theta_0 \cos\psi_0, \sin\theta_0 \sin\psi_0, \cos\theta_0)$ [40] is the initial direction vector. The scattering zenith angle θ_s and azimuth angle ψ_s for each scattering event are given by Equation (10), and the θ_s is computed by the inverse of HG function given by:

$$\begin{cases} \theta_s = \arccos \left\{ \frac{1}{2g} \left[1 + g^2 - \left(\frac{1 - g^2}{1 + g + 2g\xi_5} \right)^2 \right] \right\} \\ \psi_s = 2\pi\xi_6 \end{cases} \quad (10)$$

where ξ_5 and ξ_6 are random number uniform on [0,1].

Assume the unit direction vector of photons for pre-scattering is (μ_x, μ_y, μ_z) , the direction vector of photons for post-scattering (μ'_x, μ'_y, μ'_z) is given by [40]:

$$\begin{bmatrix} \mu'_x \\ \mu'_y \\ \mu'_z \end{bmatrix} = \begin{bmatrix} \mu_x \mu_z / \sqrt{1 - \mu_z^2} & -\mu_y / \sqrt{1 - \mu_z^2} & \mu_x \\ \mu_y \mu_z / \sqrt{1 - \mu_z^2} & \mu_x / \sqrt{1 - \mu_z^2} & \mu_y \\ -\sqrt{1 - \mu_z^2} & 0 & \mu_z \end{bmatrix} \begin{bmatrix} \sin\theta_s \cos\psi_s \\ \sin\theta_s \sin\psi_s \\ \cos\psi_s \end{bmatrix} \quad (11)$$

If $|\mu_z| \approx 1$, then Equation (11) should be replaced by:

$$\begin{bmatrix} \mu'_x \\ \mu'_y \\ \mu'_z \end{bmatrix} = \text{sign}(\mu_z) \begin{bmatrix} \sin\theta_s \cos\psi_s \\ \sin\theta_s \sin\psi_s \\ \cos\psi_s \end{bmatrix} \quad (12)$$

2.3. Photons Termination

Define Z_0 as the transmission distance, the photon is considered to have arrived at the MC computing plane ($x'O'y'$) if Inequality (13) is satisfied, and the tracing of the photon's propagation is terminated. However, as illustrated in Figure 1, the vector sum of the projections of the propagation distance of photon on the beam axis for each scattering event L_z is not always exactly equal to Z_0 . So, when $L_z > Z_0$, the arriving coordinate deviations of photons caused by ΔL should be modified by Equations (14) and (15), where (x_M, y_M, z_M) denotes the arriving coordinates of photons on the receiving plane (xOy), (x'_M, y'_M, z'_M) is the MC computing coordinates which on the $x'O'y'$ -plane.

$$L_z = z_0 + \sum_{i=1}^M \mu'_{z_i} d_i \geq Z_0 \quad (13)$$

$$\Delta L = (L_z - Z_0) / \mu'_{z_M} \quad (14)$$

$$\begin{cases} x_M = x_0 + \sum_{i=1}^M \mu'_{x_i} d_i - \Delta L \mu'_{x_M} \\ y_M = y_0 + \sum_{i=1}^M \mu'_{y_i} d_i - \Delta L \mu'_{y_M} \\ z_M = z_0 + Z_0 \end{cases} \quad (15)$$

Here, M is the total scattering order, (x_0, y_0, z_0) is the coordinates of photons emission, $(\mu'_{x_i}, \mu'_{y_i}, \mu'_{z_i})$ is the unit direction vector for the i^{th} scattering event, d_i is the propagation distance of the i^{th} scattering event, and $(\mu'_{x_M}, \mu'_{y_M}, \mu'_{z_M})$ is the unit direction vector of the photons' arrival at the receiving plane.

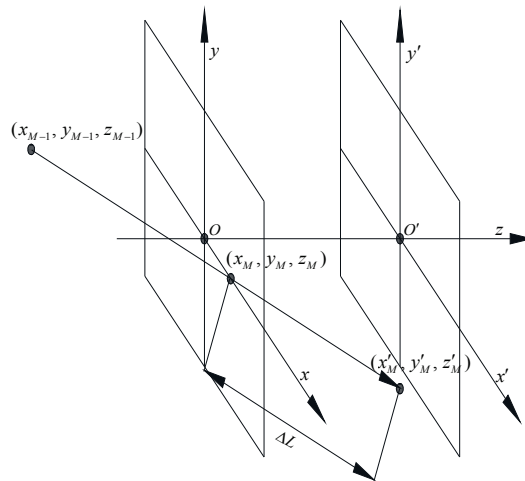


Figure 1. Schematic of arriving coordinates of photons.

2.4. Photons Reception

The receiving plane is assumed to be a square with its geometric center at the xOy -plane as the origin of the xyz coordinates system, and the laser beam axis as the z axis. The half aperture of the receiving plane is R_{PD} and the receiver’s field of view is Ψ_R . Then, the photons are considered received if Equation (16) is satisfied and the energy weight is greater than the survival threshold.

$$\begin{cases} |x_M| \leq R_{PD} \\ |y_M| \leq R_{PD} \\ L_z \geq Z_0 \\ \arccos(\mu'_{z_M}) \leq \Psi_R/2 \end{cases} \quad (16)$$

3. The 3 dB Optical Intensity Spot Radius

The 2D optical intensity distribution of the laser beam on the receiving plane can be divided into $N \times N$ components as shown in Figure 2, i.e., the receiving plane with finite dimensions is divided into $N \times N$ infinitesimal square areas, where N is a positive integer. The $N \times N$ matrix is used to store the intensity information of the laser beam and each element stores the intensity information on each infinitesimal square area. Mark this matrix as **Intensity**(\mathbf{N}, \mathbf{N}), and apply $Intensity(\eta, \zeta)$ to store the intensity distributed on the $NO.(\eta, \zeta)$ infinitesimal square area. So, the analysis for optical intensity distribution on the receiving plane can be equivalent to conducting algebraic operations on **Intensity**(\mathbf{N}, \mathbf{N}), and the total intensity is presented by Equation (17):

$$R_{Inty} = \sum_{\eta=1}^N \sum_{\zeta=1}^N Intensity(\eta, \zeta) \quad (17)$$

$$10 \lg \left(\frac{\sum_{l=N/2-N_{3dB}+1}^{N/2+N_{3dB}} \sum_{p=N/2-N_{3dB}+1}^{N/2+N_{3dB}} Intensity(l, p)}{R_{Inty}} \right) \geq -3 \quad (18)$$

Solving the minimum integer of N_{3dB} ($N_{3dB} < N/2$), which makes the Inequality (18) hold, the 3 dB OISR (r_{3dB}) which is the key parameter of this paper is given by:

$$r_{3dB} = \sqrt{2} N_{3dB} R_{PD} / N \quad (19)$$

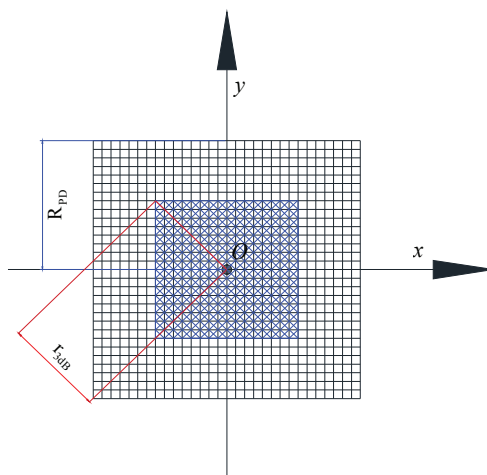


Figure 2. Schematic of optical intensity distribution and 3 dB OISR.

4. Numerical Results and Analysis

Based on the aforementioned MC simulation method and the computational principle, this paper analyzes the characteristics of the 3 dB OISR of the laser beam under various seawater channels. A laser source with a beam waist radius of 5×10^{-3} m, and divergence angle ($T - \text{Phai}$) of 1, 5 and 10 mrad is considered. It is assumed that the photons transmission velocity in seawater is $0.75 \times 2.9979 \times 10^8$ m/s, the asymmetry parameter $g = 0.924$ and simulation photons quantity is 5×10^7 . Table 2 shows the other important channel parameters used in the simulation.

Table 2. Underwater optical channel parameters based on [10].

Items	Channel Parameters			
	Pure	Clean	Coastal	Harbor
$K_a(\lambda)$ (m^{-1})	0.053	0.069	0.088	0.295
$K_s(\lambda)$ (m^{-1})	0.003	0.080	0.216	1.875
$K_{att}(\lambda)$ (m^{-1})	0.056	0.150	0.305	2.170

To study the effects of detection aperture on r_{3dB} , eight-channel types are investigated: 44 and 52 m pure seawater (Pur-44, Pur-52), 34 and 42 m clean seawater (Cle-34, Cle-42), 24 and 32 m coastal seawater (Coa-24, Coa-32) and 6 and 8 m harbor seawater (Har-6, Har-8). To further reveal the impacts of transmission distances on r_{3dB} , the transmission distances of $Z_0 \leq 160$ m, $Z_0 \leq 70$ m, $Z_0 \leq 35$ m and $Z_0 \leq 10$ m, respectively, for pure, clean, coastal and harbor seawater channel are investigated. The transmission distance is varied for different seawater channels to account for the difference in attenuation per unit distance (attenuation coefficient) (see Table 2).

To describe the trend of r_{3dB} as a function of the half-aperture of the receiving plane and transmission distance, based on the MC simulation data of r_{3dB} , the K -term Gaussian function ($K = 3, 4, 5, 6, 7$) shown by Equation (20) is utilized for curve fitting.

$$r_{3dB-Fitting}(X) = \sum_{n=1}^K a_n \exp \left[- \left(\frac{X - b_n}{c_n} \right)^2 \right] \quad (20)$$

where X denotes R_{PD} or Z_0 which depends on the MC simulation data types, the value of K is determined by the fitting accuracy, a_n , b_n and c_n are the fitting coefficients of the K -term Gaussian functions.

4.1. Pure Seawater Channel

The relations between r_{3dB} of the laser beam and R_{PD} are given by Equations (17), (19) and Inequality (18). Figure 3 presents the relations between r_{3dB} and R_{PD} for Pur-44 and Pur-52 channels. There is an approximately linear relationship between r_{3dB} and R_{PD} initially. Then the r_{3dB} saturates and hence it does not increase with the R_{PD} . The saturation effect is clearer for a small $T - \text{Phai} = 1$ and 5 mrad. This can be attributed to the fact that the role of the scattering on the laser beam intensity distribution is negligible and the beam spot size is dominantly determined by the natural divergence of the laser source. For the Pur-44 channel and the laser source with $T - \text{Phai} = 1$ mrad, the beam area can be completely collected at the receiving plane, and $r_{3dB} \approx 0.0290$ m is the saturation value if $R_{PD} \geq 0.065$ m. Figure 4 shows the 2D intensity distribution of the laser beam for $T - \text{Phai} = 1, 5$ and 10 mrad under Pur-44 and Pur-52 channels. The Gaussian characteristics expected for the laser beam are well maintained. This clearly indicates that the scattering has a negligible effect on the laser beam intensity distribution. The r_{3dB} values of the Pur-52 channel are slightly greater than the Pur-44 channel. This is expected as the longer transmission distance leads to greater divergence and hence a larger beam area.

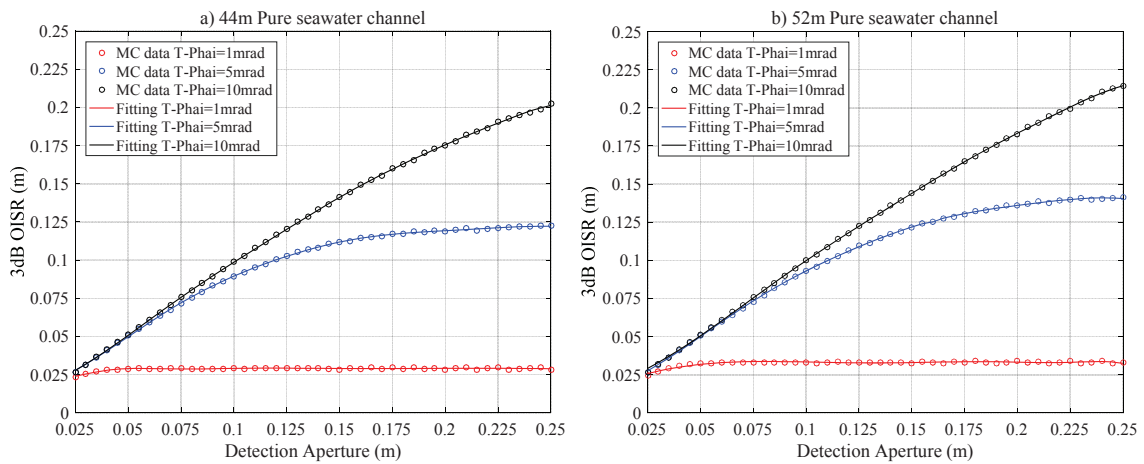


Figure 3. The r_{3dB} versus R_{PD} for pure seawater laser channel for a link distance of (a) 44 m and (b) 52 m.

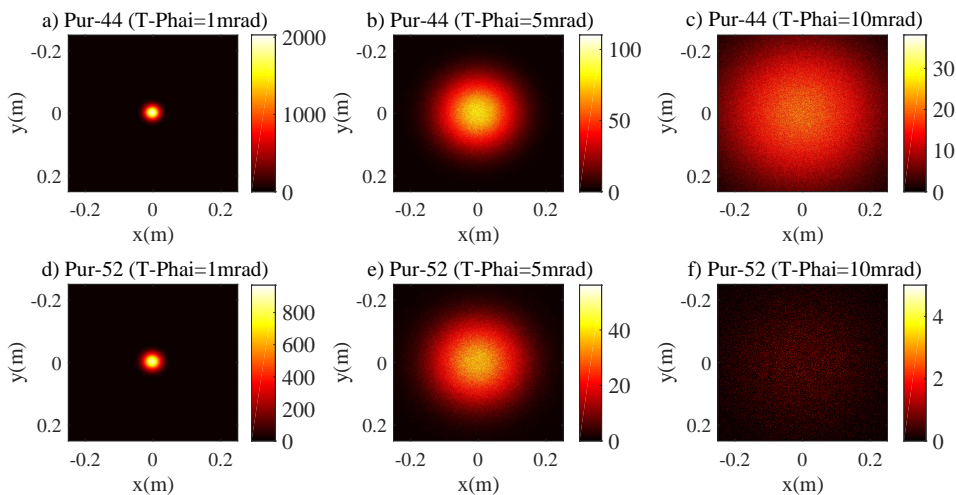


Figure 4. 2D intensity distribution of laser beam for pure seawater channel (a) Pur-44 with $T - \text{Phai} = 1$ mrad, (b) Pur-44 with $T - \text{Phai} = 5$ mrad, (c) Pur-44 with $T - \text{Phai} = 10$ mrad, (d) Pur-52 with $T - \text{Phai} = 1$ mrad, (e) Pur-52 with $T - \text{Phai} = 5$ mrad and (f) Pur-52 with $T - \text{Phai} = 10$ mrad.

Figure 5 illustrates the impacts of Z_0 on r_{3dB} . There is an approximately linear relationship between r_{3dB} and Z_0 for a very short transmission distance. Then the r_{3dB} diverges from a linear relationship, and ultimately, the r_{3dB} saturates and hence it does not increase with Z_0 . The saturation effect is clearer for T-Phai = 10 mrad, this is due to the fact that the larger divergence angle will lead to higher geometric loss, which means the receiver can only collect the center portion of the scattered and direct arrival photons. For the configurations of $R_{PD} = 0.25$ m and 0.35 m with T – Phai = 10 mrad, $r_{3dB} \approx 0.0242$ m and 0.3410 m are the saturation values for $Z_0 \geq 112$ m and 140 m, respectively. For the configurations of $R_{PD} = 0.25$ m and 0.35 m and T – Phai = 1 mrad, the two curves almost overlapped; this is due to the fact that the laser beam radius is less than 0.25 m and this makes the whole laser beam spot able to be covered by the receiver if $R_{PD} \geq 0.25$ m and $Z_0 \leq 160$ m.

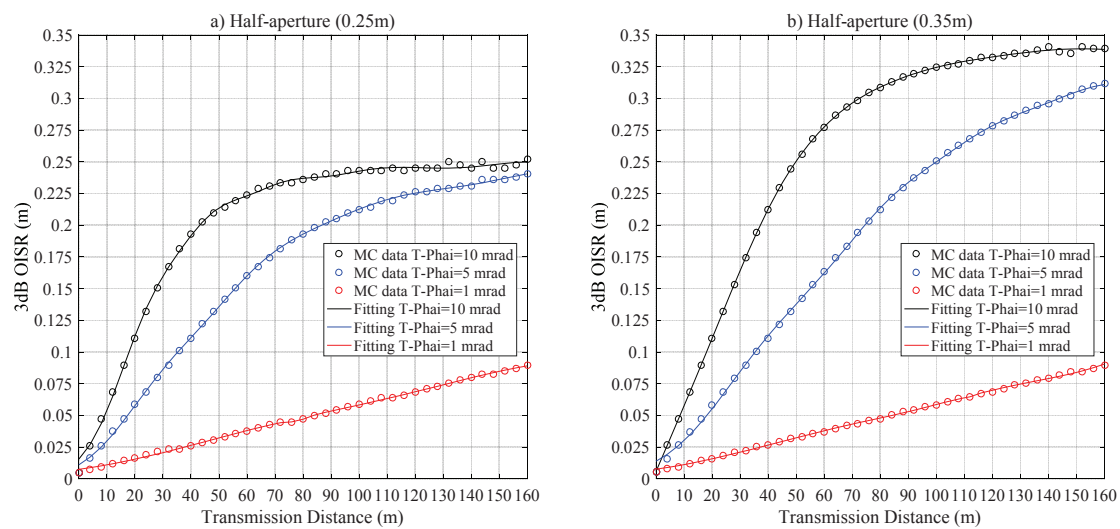


Figure 5. The r_{3dB} versus Z_0 for pure seawater laser channel for a half-aperture of (a) $R_{PD} = 0.25$ m and (b) $R_{PD} = 0.35$ m.

4.2. Clean Seawater Channel

Figure 6 characterizes the relations between r_{3dB} and R_{PD} for the Cle-34 and Cle-42 channels. The curves trend is similar to the case of the pure seawater channel. For the Cle-34 and Cle-42 channels with T – Phai = 1 mrad, $r_{3dB} \approx 0.0237$ m and 0.0280 m, respectively, are the saturation value if $R_{PD} \geq 0.075$ m. For the laser source with T – Phai = 5 mrad, these values are $r_{3dB} \approx 0.0960$ m and 0.1150 m with $R_{PD} \geq 0.175$ m and $R_{PD} \geq 0.200$ m, respectively, for the Cle-34 and Cle-42 channels. The results show that the influences of scattering on the laser beam intensity distribution are still negligible and the receiving plane can collect the whole beam spot. Figure 7 also demonstrates that 2D intensity distribution of the laser beam is Gaussian, and clearly illustrates that the scattering effects on the laser beam are insignificant. Figure 8 characterizes the the impacts of Z_0 on r_{3dB} ; the curves trend is similar to Figure 5. As in the case of the pure seawater channel, for the configurations of $R_{PD} = 0.25$ m and 0.35 m and T – Phai = 1 mrad, the two curves of r_{3dB} almost overlapped. This is due to the fact that the geometric loss still plays a very important role in r_{3dB} .

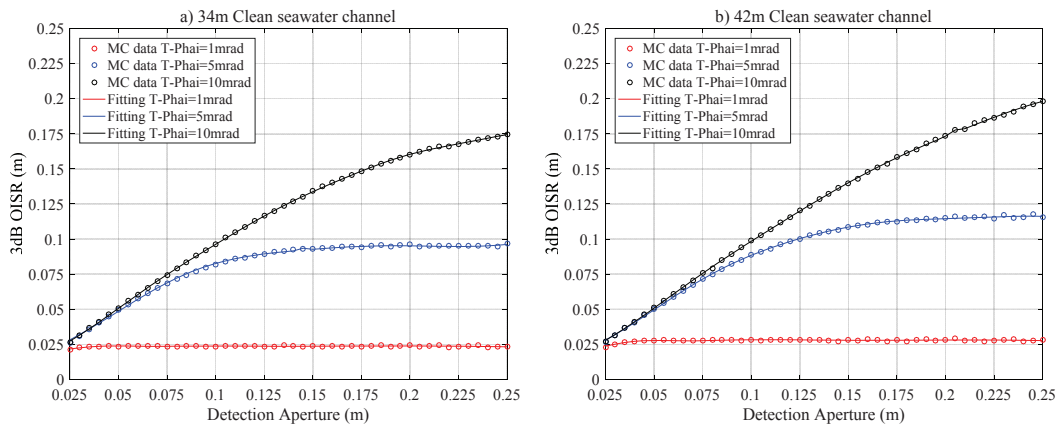


Figure 6. The r_{3dB} versus R_{PD} for the clean seawater laser channel for a link distance of (a) 34 m and (b) 42 m.

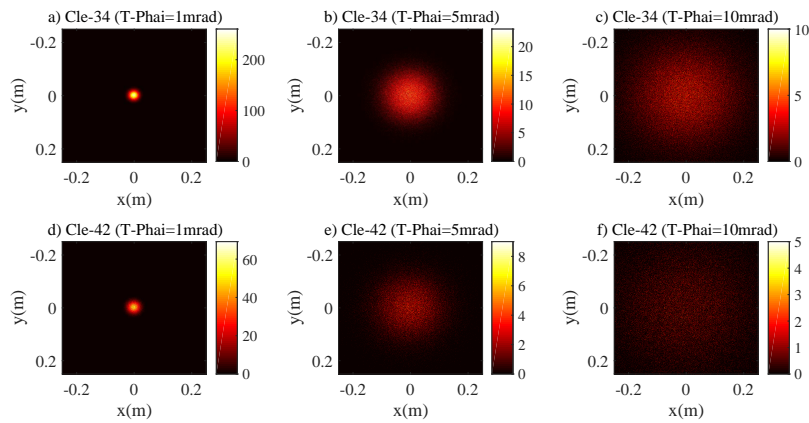


Figure 7. The 2D intensity distribution of the laser beam for the clean seawater channel (a) Cle-34 with T-Phai = 1 mrad, (b) Cle-34 with T-Phai = 5 mrad, (c) Cle-34 with T-Phai = 10 mrad, (d) Cle-42 with T-Phai = 1 mrad, (e) Cle-42 with T-Phai = 5 mrad and (f) Cle-42 with T-Phai = 10 mrad.

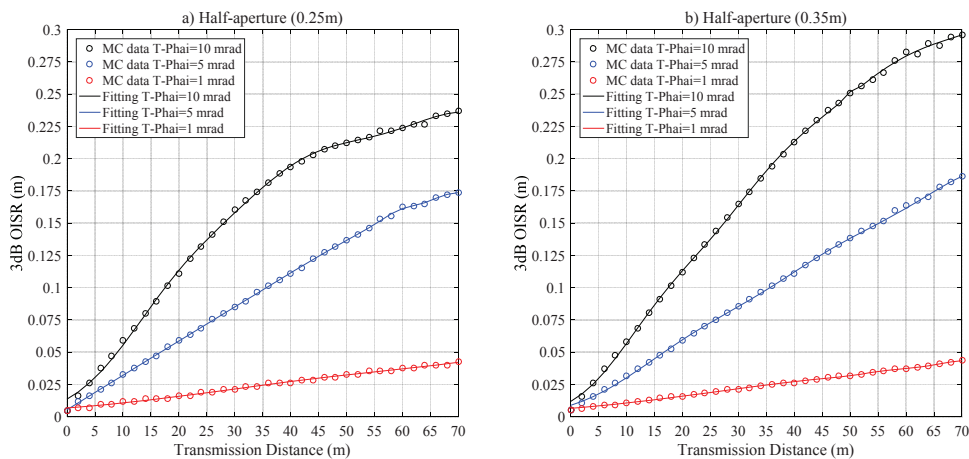


Figure 8. The r_{3dB} versus Z_0 for the clean seawater laser channel for a half-aperture of (a) $R_{PD} = 0.25$ m and (b) $R_{PD} = 0.35$ m.

4.3. Coastal Seawater Channel

Figure 9 depicts the relations between r_{3dB} and R_{PD} for the Coa-24 and Coa-32 channels. The curves trend shows a significant deviation from the previous two cases of pure and clean seawater channels. For example, for the case of the Coa-32 channel with $T - \text{Phai} = 1$ mrad, r_{3dB} diverges from a linear relationship when $R_{PD} > 0.165$ m. This is because the laser beam is scattered sparsely around the spot center, which leads to the evident increase in the r_{3dB} . For the case of $T - \text{Phai} = 5$ and 10 mrad, the curves show approximately a linearity trend initially and then saturate slowly. This is due to the consequence of increased density of scattering particles in the coastal seawater channel, resulting in a higher scattering probability of photons and causing the propagation trajectory of photons to deviate from the original direction. This leads to the non-Gaussian intensity distribution on the receiving plane. Figure 10 shows the 2D intensity distribution of the laser beam with a divergence angle of $T - \text{Phai} = 1, 5$ and 10 mrad under Coa-24 and Coa-32 channels. The figure clearly shows that Gaussian characteristics expected for the laser beam are destroyed seriously. Hence the relationship between r_{3dB} and R_{PD} is no longer similar to the cases of pure and clean seawater channels.

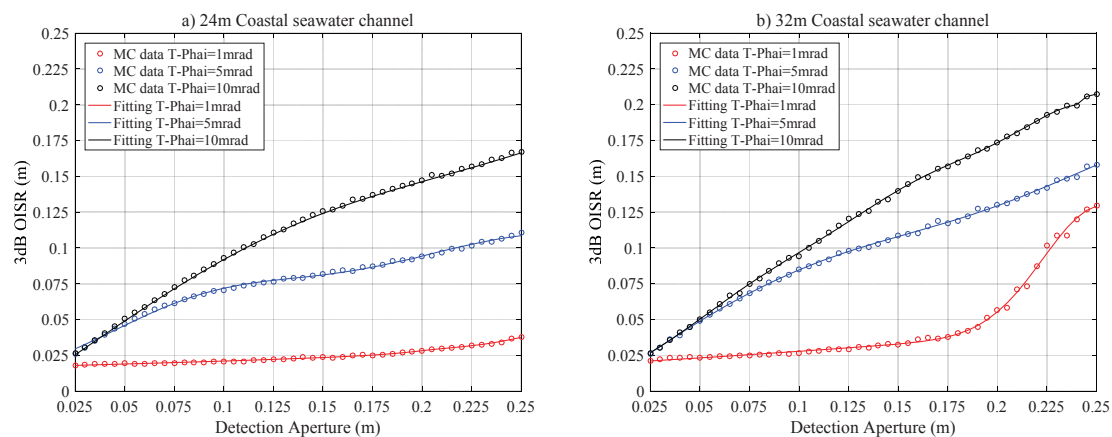


Figure 9. The r_{3dB} versus R_{PD} for the coastal seawater laser channel for a link distance of (a) 24 m and (b) 32 m.

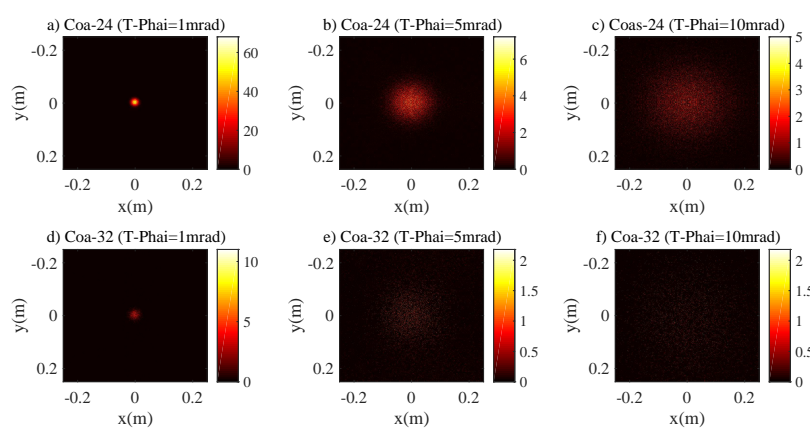


Figure 10. The 2D intensity distribution of the laser beam for coastal seawater channel (a) Coa-24 with $T - \text{Phai} = 1$ mrad, (b) Coa-24 with $T - \text{Phai} = 5$ mrad, (c) Coa-24 with $T - \text{Phai} = 10$ mrad, (d) Coa-32 with $T - \text{Phai} = 1$ mrad, (e) Coa-32 with $T - \text{Phai} = 5$ mrad and (f) Coa-32 with $T - \text{Phai} = 10$ mrad.

It is clear from Figure 11, that the curves r_{3dB} with Z_0 diverges significantly from the linear relationship for the laser beam with $T - \text{Phai} = 1$ mrad, and $r_{3dB} \approx 0.0259$ m with $Z_0 = 21$ m, $r_{3dB} \approx 0.0647$ m with $Z_0 = 14$ m are the divergence points, respectively, for $R_{PD} = 0.25$ m

and 0.35 m. The curves almost overlap for the laser beam with $T - \text{Phai} = 1$ and 5 mrad if $Z_0 \geq 25$ m with $R_{PD} = 0.35$ m. This is caused by the effects of increased scattering events, which weakens the role of geometric loss in r_{3dB} with the increase of Z_0 .

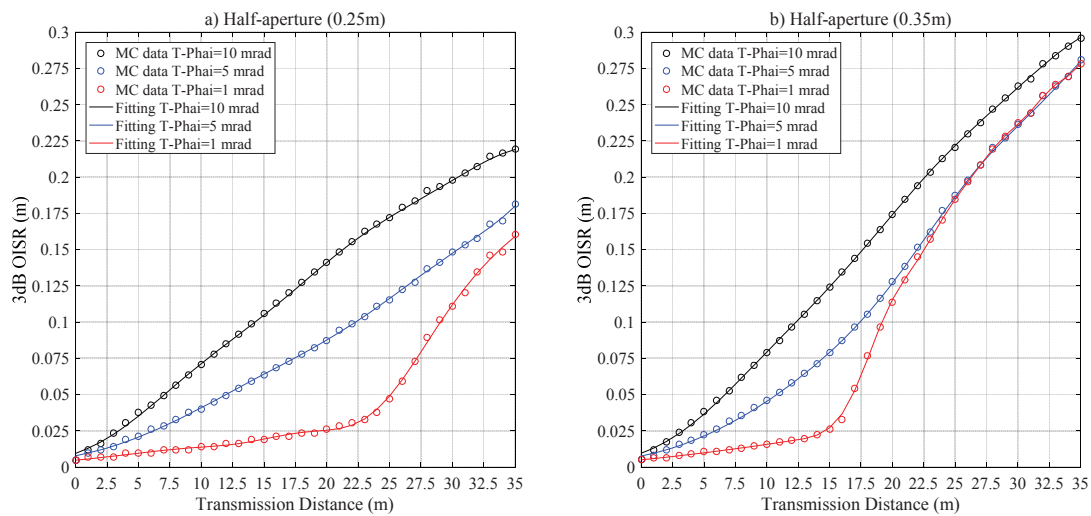


Figure 11. The r_{3dB} versus Z_0 for coastal seawater laser channel for a half-aperture of (a) $R_{PD} = 0.25$ m and (b) $R_{PD} = 0.35$ m.

4.4. Harbor Seawater Channel

Figure 12 describes the relations between r_{3dB} and R_{PD} for the Har-6 and Har-8 channels. Unlike the previous cases, the r_{3dB} does not depend on the divergence angle of the laser sources indicating the dominance of scattering in the 3 dB optical intensity spot. The harbor seawater contains a significantly higher concentration of scattering particles than the coastal seawater channel. Consequently, almost 100% of photons are scattered and hence the optical intensity at the receiving plane is randomly distributed. Figure 13 shows the 2D intensity distribution of the laser beam with the divergence angle $T - \text{Phai} = 1, 5$ and 10 mrad under Harbor channel. This shows that the 2D intensity distribution of the laser beam does not depend on the divergence angle and the intensity distribution is distributed randomly instead of Gaussian.

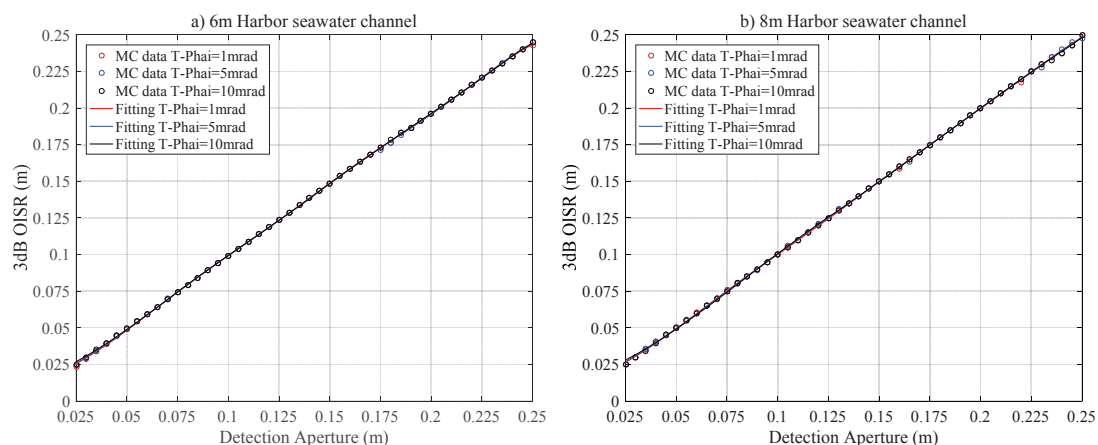


Figure 12. The r_{3dB} versus R_{PD} for harbor seawater laser channel for a link distance of (a) 6 m and (b) 8 m.

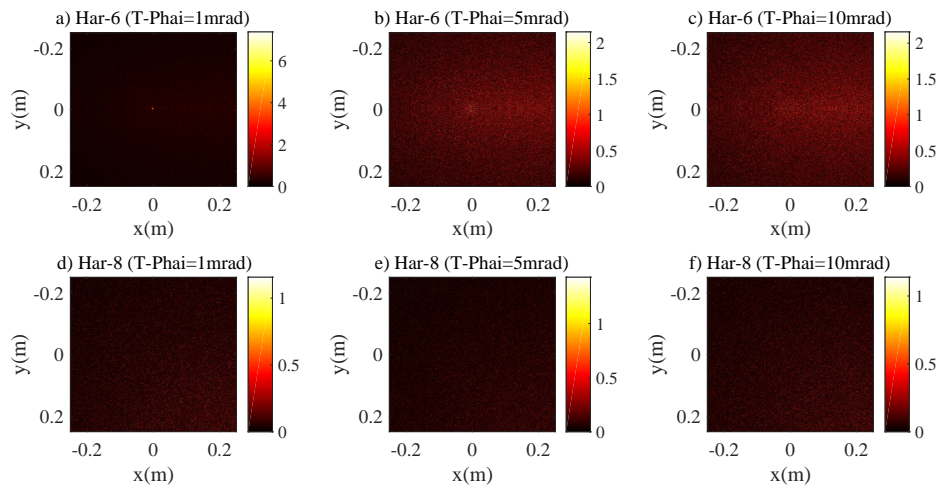


Figure 13. The 2D intensity distribution of a laser beam for harbor seawater channel (a) Har-6 with T-Phai = 1 mrad, (b) Har-6 with T-Phai = 5 mrad, (c) Har-6 with T-Phai = 10 mrad, (d) Har-8 with T-Phai = 1 mrad, (e) Har-8 with T-Phai = 5 mrad and (f) Har-8 with T-Phai = 10 mrad.

Figure 14 demonstrates the impact of Z_0 on r_{3dB} . For the configurations of $R_{PD} = 0.25$ m and 0.35 m, the difference of r_{3dB} is less than 0.0013 m and 0.0047 m, respectively; the saturation values of r_{3dB} , respectively, are 0.2498 m and 0.3485 m with $Z_0 \geq 6$ m. Additionally, to further address the 2D distribution of the laser beam in the harbor seawater channel. Figure 15 shows the relations of r_{3dB} and T – Phai, respectively, for $Z_0 = 6$ m and 10 m, which distinctly demonstrates that the divergence angle plays a negligible role in r_{3dB} .

4.5. Verification for the 3 dB Optical Intensity

The 3 dB OISR proposed in this paper is computed based on Equations (17)–(19). Hence, to verify the validity of the r_{3dB} , the attenuation loss (in dB) of total optical intensity that is covered by the r_{3dB} versus the total received optical intensity on the receiving plane is calculated. All the calculated attenuation loss values satisfy Inequality (18), and the difference is less than -2.5 dB. This shows that the calculated r_{3dB} in this paper can cover the dominating optical intensity of the laser beam.

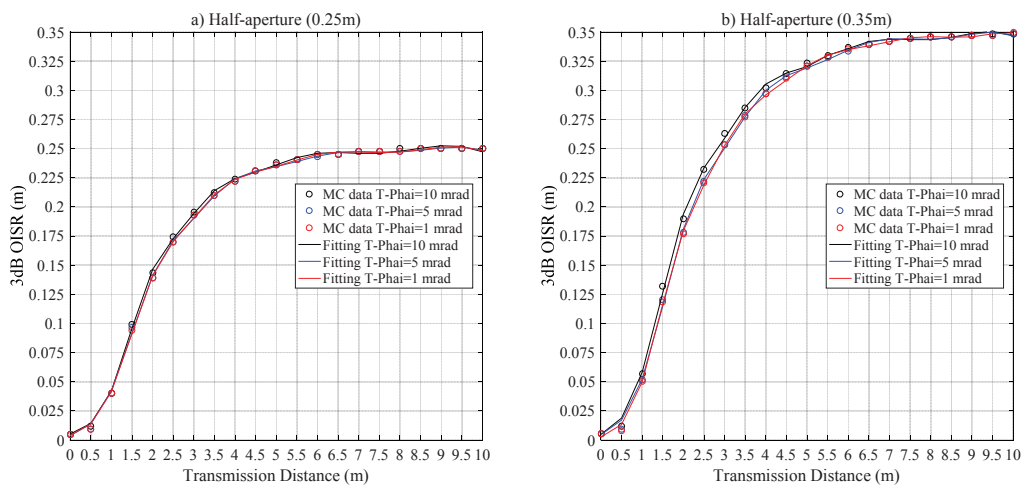


Figure 14. The r_{3dB} versus Z_0 for the harbor seawater laser channel for a half-aperture of (a) $R_{PD} = 0.25$ m and (b) $R_{PD} = 0.35$ m.

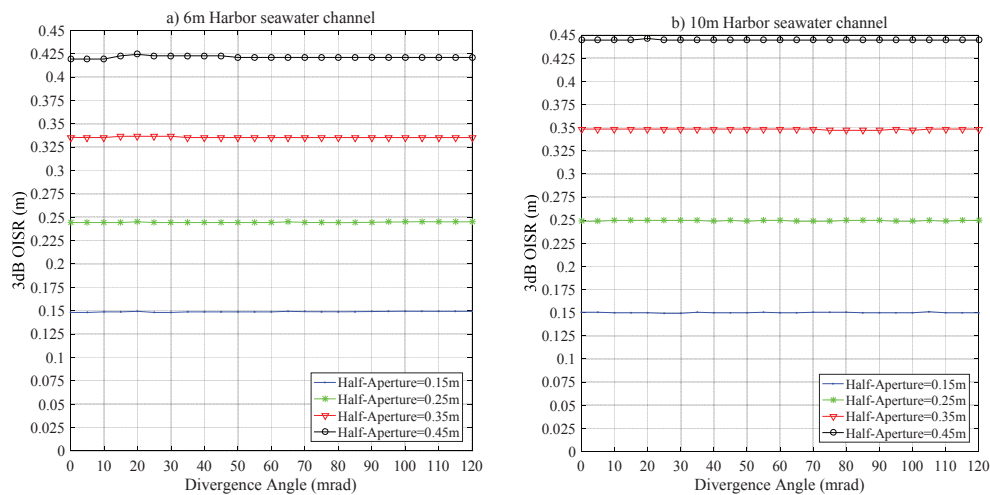


Figure 15. The r_{3dB} versus T-Phai for the harbor seawater laser channel for a link distance of (a) 6 m and (b) 10 m.

5. Conclusions

In this paper, the underwater optical channel is characterized based on optical intensity distribution and 3 dB optical intensity spot radius for the first time. The 3 dB optical intensity spot radius is an important parameter for underwater laser communication system design as most of the optical power is concentrated within this radius, and the aperture of the real optical receiver tends to be significantly smaller than the radius of the whole beam spot at the receiving plane. Hence, the 3 dB optical intensity spot radius is calculated for various underwater optical channels. In the investigation, the Henyey–Greenstein function is used to calculate the scattering angles of photons, and the influences of the underwater optical channel and optical system parameters on the 3 dB optical intensity spot radius are studied based on the Monte Carlo simulation method. The study found that there is an approximately linear relationship between r_{3dB} and R_{PD} initially for a channel with less density of scattering particles (such as clean water). Then, the r_{3dB} saturates and does not increase with the R_{PD} . Furthermore, there is approximately a linear relationship between r_{3dB} and Z_0 initially, then the r_{3dB} diverges from a linear relationship, and ultimately saturates and does not increase with the Z_0 . Additionally, the verification shows that the calculated r_{3dB} in this paper can cover the dominating optical intensity of the laser beam. For a highly scattering channel (such as the harbor channel), the optical intensity distribution is no longer a Gaussian and the effects of the divergence angle on r_{3dB} are negligible. Hence, for a highly scattering channel, the design of receiver aperture and optimal spacing of the diversity scheme for the underwater laser communication systems cannot be predicted based the divergence angle and geometric loss.

Author Contributions: Conceptualization, X.L. and W.W.; Methodology, X.L. and W.W.; Software, W.W.; Validation, X.L., S.R. and Y.L.; Formal analysis, X.L.; Investigation, X.L. and W.W.; Resources, X.L. and W.W.; Data curation, X.L. and W.W.; writing—original draft preparation, W.W. and Y.L.; Writing—review and editing, W.W. and S.R.; Visualization, W.W.; Supervision, X.L.; Project administration, X.L. and W.W.; Funding acquisition, X.L. All authors have read and agreed to the published version of the manuscript.

Funding: This research was supported by the National Natural Science Foundation of China (No. 61761014), the Foundation of Guangxi Experiment Center of Information Science (No. PT1604), the Innovation Project of Guangxi Graduate Education (No. YCSW2019152) and the GUET Excellent Graduate Thesis Program (No. 17YJPYSS38).

Conflicts of Interest: The authors declare no conflict interest.

References

1. Kaushal, H.; Kaddoum, G. Underwater optical wireless communication. *IEEE Access* **2016**, *4*, 1518–1547. [[CrossRef](#)]

2. Willner, A.E.; Zhao, Z.; Ren, Y.; Li, L.; Xie, G.; Song, H.; Liu, C.; Zhang, R.; Bao, C.; Pang, K. Underwater optical communications using orbital angular momentum-based spatial division multiplexing. *Opt. Commun.* **2018**, *19*, 21–25. [[CrossRef](#)]
3. Zeng, Z.; Fu, S.; Zhang, H.; Dong, Y.; Cheng, J. A survey of underwater wireless optical communication. *IEEE Commun. Surv. Tutor.* **2016**, *19*, 204–238. [[CrossRef](#)]
4. Jaruwatanadilok, S. Underwater wireless optical communication channel modeling and performance evaluation using vector radiative transfer theory. *IEEE J. Select. Areas Commun.* **2008**, *26*, 1620–1626. [[CrossRef](#)]
5. Cochenour, B.M.; Mullen, L.J.; Laux, A.E. Characterization of the beam-spread function for underwater wireless optical communications links. *IEEE J. Ocean. Eng.* **2008**, *33*, 513–521. [[CrossRef](#)]
6. Mullen, L.; Laux, A.; Cochenour, B. Time-dependent underwater optical propagation measurements using modulated light fields. In Proceedings of the SPIE 7317, Ocean Sensing and Monitoring, Orlando, FL, USA, 29 April 2009; pp. 1–8.
7. Mullen, L.; Laux, A.; Cochenour, B. Propagation of modulated light in water: Implications for imaging and communications systems. *Appl. Opt.* **2009**, *48*, 2607–2612. [[CrossRef](#)]
8. Mullen, L.; Laux, A.; Cochenour, B. Investigation of the effect of scattering agent and scattering albedo on modulated light propagation in water. *Appl. Opt.* **2011**, *50*, 1396–1404. [[CrossRef](#)]
9. Li, J.; Ma, Y.; Zhou, Q.; Zhou, B.; Wang, H. Channel capacity study of underwater wireless optical communications links based on Monte Carlo simulation. *J. Opt.* **2012**, *14*, 015403. [[CrossRef](#)]
10. Gabriel, C.; Khalighi, M.A.; Bourennane, S.; Léon, P.; Rigaud, V. Monte-Carlo-based channel characterization for underwater optical communication systems. *J. Opt. Commun. Netw.* **2013**, *5*, 1–12. [[CrossRef](#)]
11. Cochenour, B.; Mullen, L.; Muth, J. Temporal response of the underwater optical channel for high-bandwidth wireless laser communications. *IEEE J. Ocean. Commun. Eng.* **2013**, *38*, 730–742. [[CrossRef](#)]
12. Cox, W.; Muth, J. Simulating channel losses in an underwater optical communication system. *J. Opt. Soc. Am. Opt. Image Sci. Vis.* **2014**, *31*, 920–934. [[CrossRef](#)]
13. Liu, W.; Zou, D.; Wang, P.; Xu, Z.; Yang, L. Wavelength dependent channel characterization for underwater optical wireless communications. In Proceedings of the 2014 IEEE International Conference on Signal Processing, Communications and Computing (ICSPCC), Guilin, China, 5–8 August 2014; pp. 1–5.
14. Haltrin, V. Chlorophyll-based model of seawater optical properties. *Appl. Opt.* **1999**, *38*, 6826–6832. [[CrossRef](#)] [[PubMed](#)]
15. Li, C.; Park, K.H.; Alouini, M.S. On the use of a direct radiative transfer equation solver for path loss calculation in underwater optical wireless channels. *IEEE Wirel. Commun. Lett.* **2015**, *4*, 561–564. [[CrossRef](#)]
16. Tang, S.; Dong, Y.; Zhang, X. Impulse response modeling for underwater wireless optical communication links. *IEEE Trans. Commun.* **2014**, *62*, 226–234. [[CrossRef](#)]
17. Zhang, H.; Dong, Y. Impulse response modeling for general underwater wireless optical MIMO links. *IEEE Commun. Mag.* **2016**, *54*, 56–61. [[CrossRef](#)]
18. Zhang, H.; Dong, Y. General stochastic channel model and performance evaluation for underwater wireless optical links. *IEEE Trans. Wirel. Commun.* **2016**, *15*, 1162–1173. [[CrossRef](#)]
19. Wang, C.; Yu, H.Y.; Zhu, Y.J. A long distance underwater visible light communication system with single photon avalanche diode. *IEEE Photonics J.* **2016**, *8*, 7906311. [[CrossRef](#)]
20. Huang, A.P.; Tao, L.W. Monte Carlo based channel characteristics for underwater optical wireless communications. *IEICE Trans.* **2017**, *E100-B*, 612–618. [[CrossRef](#)]
21. Dong, F.; Xu, L.; Jiang, D.; Zhang, T. Monte-Carlo-based impulse response modeling for underwater wireless optical communication. *Prog. Electromagn. Res.* **2017**, *54*, 137–144. [[CrossRef](#)]
22. Oubei, H.M.; Zedini, E.; ElAfandy, R.T.; Kammoun, A.; Abdallah, M.; Ng, T.K.; Hamdi, M.; Alouini, M.S.; Ooi, B.S. Simple statistical channel model for weak temperature-induced turbulence in underwater wireless optical communication systems. *Opt. Lett.* **2017**, *42*, 2455–2458. [[CrossRef](#)]
23. Vali, Z.; Gholami, A.; Ghassemlooy, Z.; Michelson, D.G.; Omoomi, M.; Noori, H. Modeling turbulence in underwater wireless optical communications based on Monte Carlo simulation. *J. Opt. Soc. Am. A* **2017**, *34*, 1187–1193. [[CrossRef](#)] [[PubMed](#)]
24. Liu, T.; Zhang, H.; Song, J. Monte-Carlo simulation-based characteristics of underwater scattering channel. *Opt. Eng. Lett.* **2017**, *56*, 070501. [[CrossRef](#)]

25. Qadar, R.; Kasi, M.K.; Ayub, S.; Kakar, F.A. Monte Carlo-based channel estimation and performance evaluation for UWOC links under geometric losses. *Int. J. Commun. Syst.* **2018**, *31*, e3527. [[CrossRef](#)]
26. Jasman, F.; Zaiton, A.M.; Ahmad, Z.; Rihawi, Z. Scattering regimes for underwater optical wireless communications using Monte Carlo simulation. *Int. J. Elect. Comput. Eng.* **2018**, *8*, 2571–2577. [[CrossRef](#)]
27. Sahu, S.K.; Shanmugam, P. A theoretical study on the impact of particle scattering on the channel characteristics of underwater optical communication system. *Opt. Commun.* **2018**, *408*, 3–14. [[CrossRef](#)]
28. Jamali, M.V.; Mirani, A.; Parsay, A.; Abolhassani, B.; Nabavi, P.; Chizari, A.; Khorramshahi, P.; Abdollahramezani, S.; Salehi, J.A. Statistical studies of fading in underwater wireless optical channels in the presence of air bubble, temperature, and salinity random variations. *IEEE Trans. Commun.* **2018**, *66*, 4706–4723. [[CrossRef](#)]
29. Li, Y.; Lesson, M.S.; Li, X. Impulse response modeling for underwater optical wireless channel. *Appl. Opt.* **2018**, *57*, 4815–4823. [[CrossRef](#)]
30. Farshad, M.; Murat, U. Visible light communication channel modeling for underwater environments with blocking and shadowing. *IEEE Access* **2018**, *6*, 1082–1090.
31. Mohammed, E.; Farshad, M.; Murat, U. Performance characterization of underwater visible light communication. *IEEE Trans. Commun.* **2019**, *67*, 543–552.
32. Zedini, E.; Oubei, H.M.; Kammoun, A.; Hamdi, M.; Ooi, B.S.; Alouini, M.S. Unified statistical channel model for turbulence-induced fading in underwater wireless optical communication systems. *IEEE Trans. Commun.* **2019**, *67*, 2893–2907. [[CrossRef](#)]
33. Roumelas, G.D.; Nistazakis, H.E.; Stassinakis, A.N.; Volos, C.K.; Tsigopoulos, A.D. Underwater optical wireless communications with chromatic dispersion and time jitter. *Computation* **2019**, *7*, 35. [[CrossRef](#)]
34. Saxena, P.; Bhatnagar, M.R. A simplified form of beam spread function in underwater wireless optical communication and its applications. *IEEE Access* **2019**, *7*, 105298–105313. [[CrossRef](#)]
35. Illi, E.; Bouanani, F.E.; Park, K.H.; Ayoub, F.; Alouini, M.S. An improved accurate solver for the time-dependent RTE in underwater optical wireless communications. *IEEE Access* **2019**, *7*, 96478–96494. [[CrossRef](#)]
36. Hufnagel, F.; Sit, A.; Grenapin, F.; Bouchard, F.; Heshami, K.; England, D.; Zhang, Y.; Sussman, B.J.; Boyd, R.W.; Leuchs, G.; et al. Characterization of an underwater channel for quantum communications in the Ottawa River. *Opt. Express* **2019**, *27*, 26346–26354. [[CrossRef](#)]
37. Sait, M.; Sun, X.; Alkhazragi, O.; Alfaraj, N.; Kong, M.; Ng, T.K.; Ooi, B.S. The effect of turbulence on NLOS underwater wireless optical communication channels. *Chin. Opt. Lett.* **2019**, *17*, 100013. [[CrossRef](#)]
38. Mobley, C.D.; Sundman, L.K.; Boss, E. Phase function effects on oceanic light fields. *Appl. Opt.* **2002**, *41*, 1035–1050. [[CrossRef](#)]
39. Mobley, C.D. *Light and Water: Radiative Transfer in Natural Waters*; Academic Press: Pittsburgh, PA, USA, 1994.
40. Leathers, R.A.; Downes, T.V.; Davis, C.O.; Mobley, C.D. *Monte Carlo Radiative Transfer Simulations for Oceanoptics: A Practical Guide*; Naval Reserch Laboratory: Washington, DC, USA, 2004.
41. Cox, W. *Simulation, Modeling, and Design of Underwater Optical Communication Systems*; North Carolina State University: Raleigh, NC, USA, 2012.

